"Laser Techniques for State-Selected and State-to-State Chemistry"

Proc. SPIE - Int. Conf. Opt. Eng. Vol. 2124 (1994).

Photofragment imaging of angle-velocity distributions

Robert A. Hertz and Jack A. Syage

The Aerospace Corporation
P.O. Box 92957/M5-754
Los Angeles, California 90009

ABSTRACT

Photofragment angle-velocity distributions are measured in a molecular beam using a new two-dimensional imaging technique. We report on the detection of weak perpendicular transitions for CH_3I $\tilde{A}$ state photodissociation at 266 and 304 nm. The ratio of cross sections and the $^3Q_0 - {}^1Q$ crossing probability are $\sigma_\perp/\sigma_{||} = 0.00 - 0.10$ and $p = 0.22 - 0.27$ at 266 nm and $\sigma_\perp/\sigma_{||} = 0.20 - 0.30$ and $p = 0.43 - 0.48$ at 304 nm.

1. INTRODUCTION

Detailed information on the ultrafast dynamics of photodissociation can often be gained by measurements of the kinetic energy (velocity) and angular dependence of the photofragments.[1–7] In this account we describe a new molecular beam technique for directly recording two-dimensional images (i.e., in-plane slices rather than projections) of the three-dimensional product angle-velocity distribution. This method holds important advantages over existing techniques that must process experimental data to extract the center-of-mass (c.m.) angle-velocity distributions. Photofragment translational energy spectroscopy yields a 2D angle-velocity distribution, but requires a laboratory to c.m. transformation that varies with product velocity, thus requiring forward convolution routines.[1,2] Translational energy can also been measured in a time-of-flight mass spectrometer.[3–7] In an interesting adaptation, Chandler and Houston imaged the ion packet spatial distribution using a microchannel plate intensified camera system.[7] This method records a 2D projection of a 3D angle-velocity distribution that must be inverted by an Abel transformation in order to obtain an in-plane 2D distribution.

2. BACKGROUND

The $\tilde{A}$ states of CH_3I are due to $5pn \rightarrow \sigma^*$ excitations that are split by spin-orbit interactions into five components. Transitions to three component states are electric-dipole allowed from the ground electronic state and are denoted in order of increasing energy as $^3Q_1$, $^3Q_0$, and ^1Q (Mulliken notation, $2E$, $2A$, and $3E$ in C_{3v} symmetry).[8] Potential energy curves calculated by Tadjeddine *et al.*[9] are presented in Fig. 1. The $^3Q_1$ and ^1Q states are reached by transition moments perpendicular to the C–I bond and the $^3Q_0$ state by a parallel transition moment. The perpendicular transitions correlate to the $CH_3 + I(^2P_{3/2})$ dissociative limit and the parallel transition correlates to the $CH_3 + I^*(^2P_{1/2})$ limit.[8–11] These simple considerations predict a crossing of the $^3Q_0$ and ^1Q surfaces.

The angular distribution of photofragments is given by the expression

$$\frac{d\sigma}{d\Omega} = \frac{\sigma}{4\pi}\left[1 + \frac{\beta}{2}\left(3\cos^2\theta - 1\right)\right] \tag{1}$$

where σ is the absorption cross section, θ is the fragment ejection angle relative to the laser polarization

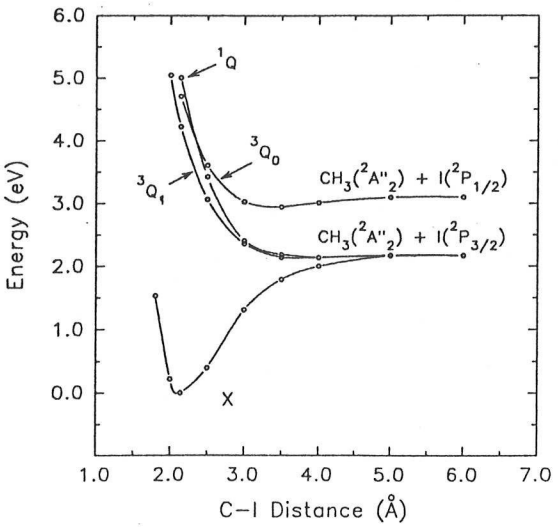

Figure 1. Potential energy curves for the ground electronic state $\tilde{X}$ and the optically active dissociative $\tilde{A}$ states. Symbols are calculated values from Tadjeddine *et al.* (Ref. 9a).

axis, and β is the anisotropy parameter, which is -1 or $+2$ for directly dissociative perpendicular and parallel transitions, respectively. If molecular rotation occurs during the lifetime of the excited state, then β will have a value between the above limits. Evidence to date indicates that the $\tilde{A}$ state lifetime is on the order of 100 fs.[1–5,12] In the diabatic picture of the $\tilde{A}$ state potentials, one would expect I and I* to be produced with angular distributions corresponding to β values of -1 and 2, respectively (i.e., angular distributions peaking perpendicular to and parallel to the laser polarization axis, respectively). Instead, photofragment anisotropy measurements show that both I and I* exhibit parallel-like dissociation.[1–5] These results are explained by a dominant parallel transition to $^3Q_0$ that undergoes a branching at the $^3Q_0 - {}^1Q$ surface crossing to give I and I* (Fig. 1). Calculations support this interpretation.[9–11] Butler and coworkers presented experimental evidence for the surface crossing and branching by showing that the emission polarization from $\tilde{A}$ state excitation evolves from a pure parallel component to a mixture of parallel and perpendicular components.[13]

The crucial issues that we address here are (1) the relative importance of the perpendicular states leading to $I(^2P_{3/2})$ due to direct excitation versus due to surface crossing, (2) the surface crossing probability, and (3) the dependence of these properties on photolysis wavelength.

3. EXPERIMENTAL METHODS

The method of recording 2D images of 3D angle-velocity distributions is illustrated in Fig. 2. Photodissociation is initiated and products subsequently ionized by laser excitation. The expanding ion packet (shown as a sphere in Fig. 2 for clarity) represents the 3D angle-velocity distribution. A series of time-of-flight spectra are collected using a rastering procedure that sweeps the ionized photoproduct packet across the detector aperture by electric field deflection.

The velocity components in a specific plane of interest are dispersed temporally along the z-axis and spatially along either the x- or y- axis. The c.m. velocity components in the laboratory axis system are given by the relations

$$v_z = \frac{q\epsilon(t_0 - t)}{m} \tag{2}$$

$$v_{x,y} = \frac{l}{t_0} = \frac{1}{t_0}(KV_{defl}) \tag{3}$$

Syage

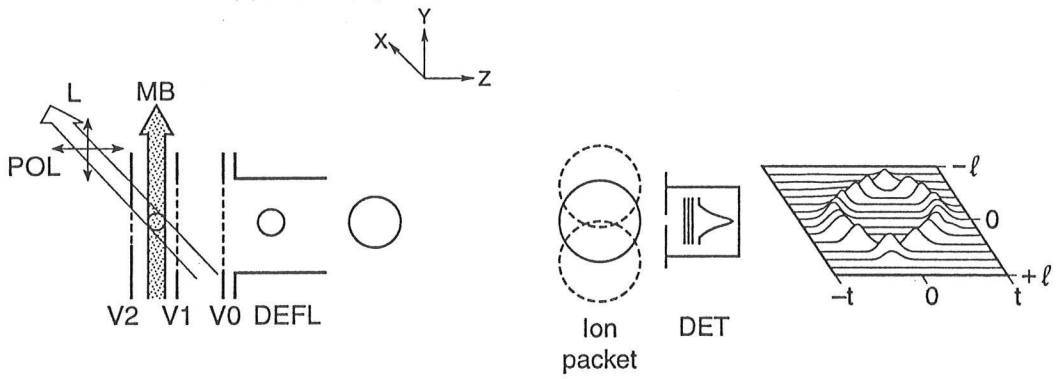

Figure 2. Time-of-flight ion optics assembly used for measuring photofragment angle-velocity distributions. Terms are defined as follows: DEFL - ion deflector plates, DET - detector; L - laser, MB - molecular beam; POL - laser polarization axis; V0, V1, V2 - ion acceleration grids. Deflector plates for x-axis is not shown. The simulated spectrum is shown in temporal, t and spatial l coordinates, which correlate directly with product velocity.

Eq. (2) assumes two-stage ion acceleration under space focussing conditions[14] where ϵ is the extraction field, q is charge, m is mass, and $t - t_0$ is the arrival time relative to the center of the distribution t_0.[15] In Eq. (3) K is a constant relating the deflector voltage V_{defl} to the spatial deflection l at the detector. Our time-of-flight mass spectrometer consists of an ion optics assembly of three grids V0–V2 each separated by 1 cm, a one-meter drift tube, and an 18-mm diam microchannel plate detector in front of which is mounted a 5-mm diam aperture. The results presented here were collected using 15 V/cm and 230 V/cm for the extraction and acceleration fields, respectively. Under these operating conditions, I^+ ions have flight times centered at $t_0 = 72$ μs. A combination of the detector aperture diameter and blurring of the ion image due to diffraction off grids currently limits our spatial resolution to about 8-10 mm. The ion packet for I^+ expands to about 80 mm diam at the detector, corresponding to an acceptance angle of about $\pm 7^o$ for the highest velocity group, which increases for decreasing velocity.

Photofragment images are recorded in the xz and yz planes and laser polarization P is aligned along either the z-axis or y-axis (denoted P_z and P_y). The c.m. velocity components in the xyz laboratory axis system are uvw for P_z polarization and uwv for P_y polarization. The xz and yz planes of detection correspond to the uw and vw velocity components for P_z and the uv and wv velocity components for P_y. Hence three orthogonal planes of detection are available. The vw and wv planes of detection are redundant and provide a consistency check for measuring velocity along the spatial y and temporal z laboratory axes.

Photolysis was initiated at 266 nm or 304 nm. I and I* photofragment were ionized by 2+1 resonance enhanced multiphoton ionization (REMPI) using 304.7 and 304.0 nm excitation, respectively.[16] Laser pulse energies and focussing conditions were adjusted to avoid space charge repulsion and in the case of 266-nm photolysis to maximize the two-pulse signal relative to the one-color signal. The two-color signal for 266-nm photolysis and 304 nm ionization was at least a factor of 20 greater than the ion signal by either pulse alone. TOF spectra were collected using a LeCroy 9450 digital scope. Individual traces comprising an image were averaged over 2000 pulses. Complete images, therefore, represent about 30 minutes of data acquisition time at 10-Hz operation. In future work we hope to operate in ion counting mode using a multihit time-to-amplitude converter, which should improve dramatically sensitivity and dynamic range.

The CH_3I sample was placed in a bubbler cooled to 0°C and delivered to the pulsed valve by a flow of Ar or He at 400 psi (results were unchanged at lower temperatures). To inhibit cluster excitation, the pulsed valve was heated to 60°C and excitation was synchronized to the leading edge of the gas pulse.

Syage

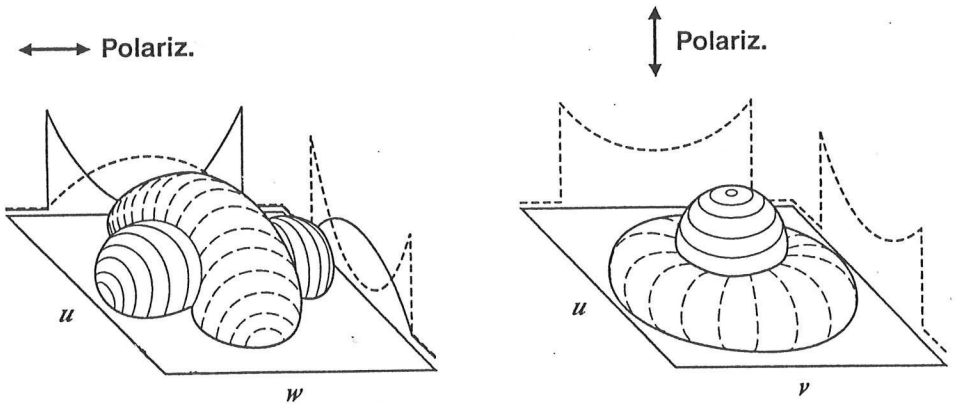

Figure 3. Representation of the angular probabilities for photofragment ejection angle arising from parallel (—) and perpendicular (- - -) transitions of CH_3I. Two planes of detection chosen to selectively probe these two transitions are shown along with calculated 1D projections of the 2D angle-velocity images. u, v, and w are orthogonal c.m. velocity components.

Cluster formation was negligible under these conditions as verified by low energy electron impact mass spectra and corroborated in the angle-velocity images by the absence of the characteristic low energy I atoms from cluster photodissociation.[3]

RESULTS

For axisymmetric systems only two planes of detection are needed. We choose the xz laboratory frame, which corresponds to the uw and uv velocity planes for P_z and P_y, respectively. The product angular distributions expected for directly dissociating parallel and perpendicular transitions ($\beta = 2$ and -1, respectively) are illustrated in Fig. 3. The 1D projections of the 2D images are also shown. *The uv plane is especially important because it probes in the node of the parallel angular distribution and, therefore, is very sensitive to detecting perpendicular transitions.*

The uw and uv image planes were recorded for I and I* (304.7 and 304.0 nm probe excitation by 2+1 resonance enhanced multiphoton ionization, REMPI) for 266 and 304-nm photolysis. The results for 266-nm and 304-nm photolysis and I atom probe are shown in Figs. 4 and 5. A strong forward-backward peaked angular distribution is observed in Figs. 4a and 5a for the uw plane, corresponding to the direct dissociation from a dominant parallel transition. The uv planes in Figs. 4b and 5b, on the other hand, show the characteristic "donut" shaped angular distribution expected for a perpendicular transition.

Angle and velocity resolution by this method are favored by fragments that carry high recoil velocity as this leads to greater spreading of the ion packet before reaching the detector. The velocity of I atom is given by $v_I^2 = (\epsilon_t/m_I)(m_{CH_3}/m_{CH_3I})$ where ϵ_t is c.m. kinetic energy and m is mass. From this standpoint, the photodissociation of CH_3I is a poor system for highlighting the performance of the present technique because of the disadvantages of detecting a heavy fragment I and being matched to a light fragment CH_3. These unfavorable kinematics account for the $\geq \pm 7^o$ fragment acceptance angle explained in the Experimental. As a result about 6% of ions from parallel excitation, those with near orthogonal scattering angles, are calculated to appear in the uv image plane that we reserve for detection of ions from perpendicular transitions. Parallel contributions to the weak 266-nm perpendicular image are evident in Fig. 4b, particularly in the 1D projection for u, in which intensity has filled in at $u = 0$. The perpendicular image at 304 nm in Fig. 5b is less affected by the parallel transition due to the larger value of the cross section ratio $\sigma_\perp/\sigma_{||}$ at 304 nm versus 266 nm. Despite these uncertainties exemplary results are obtained, which should indicate the potential resolution possible for more general cases of

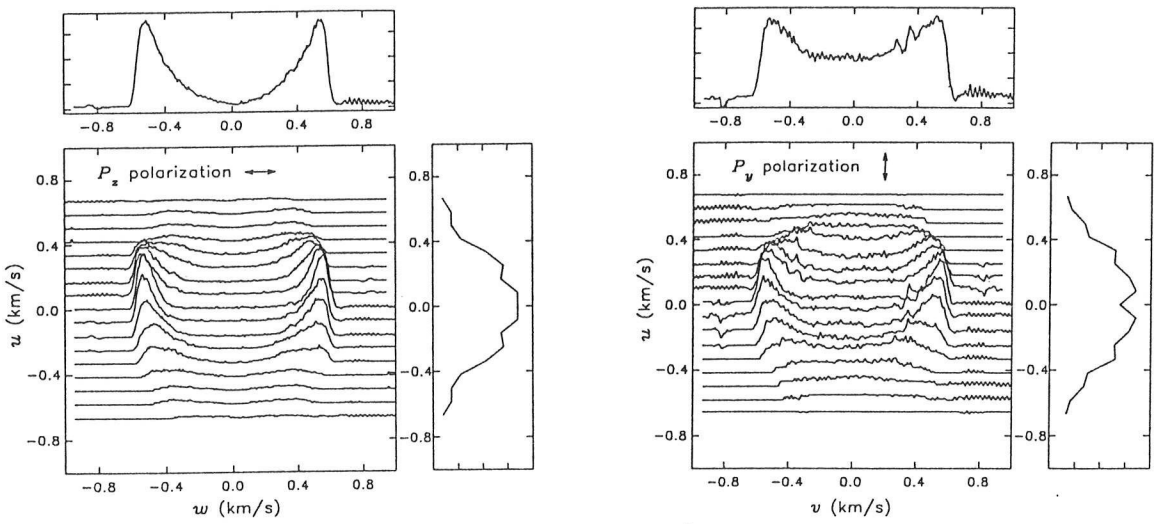

Figure 4. Measurements of the 2D angle-velocity images of the I atom fragment from photodissociation of CH_3I at 266 nm. Shown are images in planes that selectively probe the parallel and perpendicular transitions, respectively, along with their 1D projections obtained by summing the TOF spectra along the one axis (see Fig. 3). The ordinate of the 2D plot denotes the u value for each TOF trace. Intensity should be viewed as orthogonal to the uw and uv planes.

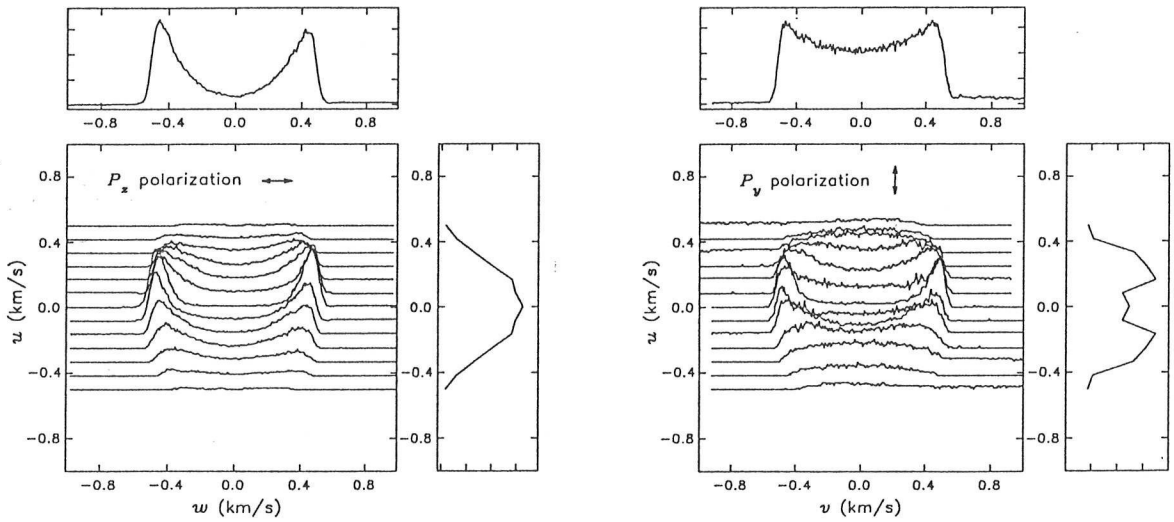

Figure 5. Measurements of the 2D angle-velocity images of the I atom fragment from photodissociation of CH_3I at 304 nm. See caption to Fig. 4.

photodissociation. In addition, system upgrades are planned that should improve spatial resolution by a least a factor of two.

Individual high sensitivity TOF spectra were also recorded along the image centerline at $u = 0$. These spectra correspond to scattering through angles of $\theta = 0^o$ [$I_{||}(w)$ trace] and $\theta = 90^o$ [$I_{\perp}(v)$ trace]. The ratio of total intensity $I_{\perp}/I_{||}$ is 0.00–0.05 at 266 nm and 0.10–0.15 at 304 nm, after subtracting the ion signal from parallel excitation that leaks into the perpendicular plane of detection. These values correspond to β values of 1.7–2.0 and 1.3–1.5, respectively. The perpendicular component was barely discernable for I* detection as expected for a product that correlates with the strong parallel $^3Q_0$ state.

TABLE I. Measurement of cross section ratio, branching ratio, and surface crossing probability.

λ	$\sigma_\perp/\sigma_\parallel$	I/I*	p
266 nm	0.00–0.10	0.37[a]	0.22–0.27
304 nm	0.20–0.30	1.3	0.43–0.48

[a] From Ref. 18

DISCUSSION

The ratio of cross sections for perpendicular and parallel transitions is straightforward to determine. Eq. (1) leads to the simple expression $\sigma_\perp/\sigma_\parallel = 2I_\perp/I_\parallel$. Our measurements for I($^2P_{3/2}$) lead to $\sigma_\perp/\sigma_\parallel$ ratios of 0.00–0.10 at 266 nm and 0.20–0.30 at 304 nm. Gedanken and Rowe recorded absorption and magnetic circular dichroism (MCD) spectra of CH_3I, from which they determined the $^3Q_1$, $^3Q_0$, and ^1Q component contributions to the continuum $\tilde{A}$ band absorption.[17] The peak component absorption wavelengths are reported to be 300, 261, and 240 nm, respectively, and the percentage total absorption strengths are 1:78:21, respectively. The MCD results indicate a minimum in $\sigma_\perp/\sigma_\parallel$ at 260 nm, which is consistent with our results. At 304 nm the ratio of the weak $^3Q_1$ band to the far wing of the strong $^3Q_0$ band is difficult to access from the MCD results.

The surface crossing probability p can be determined from measurements of $\sigma_\perp/\sigma_\parallel$ and the branching ratio $f(\mathrm{I})/f(\mathrm{I}^*)$. Product yield can be expressed by

$$\begin{pmatrix} f(I) \\ f(I^*) \end{pmatrix} = \begin{pmatrix} 1-p & p & 1 \\ p & 1-p & 0 \end{pmatrix} \cdot \begin{pmatrix} \sigma_\perp(^1Q) \\ \sigma_\parallel(^3Q_0) \\ \sigma_\perp(^3Q_1) \end{pmatrix} \tag{4}$$

where we assume a crossing probability for the ^1Q and $^3Q_0$ surfaces, but not for the $^3Q_1$ surface, which lies at lower energy. The analysis simplifies considerably by assuming, based on theory[11] and MCD spectra,[17] that $\sigma_\perp(^1Q) \gg \sigma_\perp(^3Q_1)$ at 266 nm and $\sigma_\perp(^1Q) \ll \sigma_\perp(^3Q_1)$ at 304 nm. A value of $f(\mathrm{I})/f(\mathrm{I}^*) = 0.37$ at 266 nm has been measured previously,[18] which in combination with the measured cross section ratio $\sigma_\perp/\sigma_\parallel$ in Table I yields a value for the crossing probability p of 0.22–0.27. We estimate a value of $f(\mathrm{I})/f(\mathrm{I}^*) = 1.3$ at 304 nm by scaling the branching ratio at 266 nm by the relative signal intensities of I and I* at the two wavelengths. An early photoacoustic study reports a value of about 2.0.[19] Using our branching ratio and cross section ratio yields a crossing probability of 0.43–0.48 at 304 nm. A summary of these values is given in Table I.

Shapiro calculated crossing probabilities from the parallel transition of about 0.32 and 0.50 for 266 and 304 nm, respectively.[11] Though somewhat larger than the observed values, they exhibit the trend observed here that p increases with decreasing energy. Shapiro attributes this effect to the energy released into translation; the less translational energy, the slower is the passage through the crossing region, and consequently, the greater is the crossing probability.

SUMMARY

The principal result here is the demonstration of a new photofragment imaging technique that delivers

direct c.m. in-plane 2D images (as opposed to projections) of 3D angle-velocity distributions. We have confirmed the existence of the weak ^1Q and $^3Q_0$ perpendicular transitions that overlap with the strong $^3Q_0$ parallel transition that make up the $\tilde{A}$ state continuum and determined relative cross sections and curve crossing probabilities at 266 and 304 nm. The efficiency of our imaging technique should make it possible to generate a valuable data base, at several wavelengths, of branching ratios, β dependences, more accurate component cross sections and curve crossing probabilities, and vibrational distributions of the counter fragment (e.g., CH_3 in the case of CH_3I).

REFERENCES

1. R. K. Sparks, K. Shobatake, L. R. Carlson, and Y. T. Lee, *J. Chem. Phys.* **75,** 3838 (1981).
2. G. N. A. van Veen, T. Baller, A. E. de Vries, and N. J. A. van Veen, *Chem. Phys.* **87,** 405 (1984). M. D. Barry and P. A. Gorry, *Mol. Phys.* **52,** 461 (1984).
3. R. Ogorzalek Loo, H.-P. Haerri, G. E. Hall, and P. L. Houston, *J. Chem. Phys.* **90,** 4222 (1989); R. Ogorzalek Loo, G. E. Hall, H.-P. Haerri, and P. L. Houston, *J. Phys. Chem.* **92,** 5 (1988).
4. S. M. Penn, C. C. Hayden, K. J. Carlson Muyskens, and F. F. Crim, *J. Chem. Phys.* **89,** 2909 (1988).
5. J. F. Black and I. Powis, *Chem. Phys.* **125,** 375 (1988).
6. H. J. Hwang and M. A. El-Sayed, *J. Phys. Chem.* **96,** 8728 (1992); H. J. Hwang and M. A. El-Sayed, *J. Chem. Phys.* **94,** 4877 (1991).
7. D. W. Chandler and P. L. Houston, *J. Chem. Phys.* **87,** 1445 (1987). D. W. Chandler, J. W. Thoman, Jr., M. H. M. Janssen, and D. H. Parker, *Chem. Phys. Lett.* **156,** 151 (1989).
8. R. S. Mulliken, *J. Chem. Phys.* **8,** 382 (1940); *ibid.* **3,** 513 (1935).
9. M. Tadjeddine, J. P. Flament, and C. Teichteil, *Chem. Phys.* **118,** 45 (1987).
10. S. K. Gray and M. S. Child, *Mol. Phys.* **51,** 189 (1984).
11. M. Shapiro, *J. Phys. Chem.* **90,** 3644 (1986).
12. J. L. Knee, L. R. Khundkar, and A. H. Zewail, *J. Chem. Phys.* **83,** 1996 (1985).
13. K. Q. Lao, M. D. Person, P. Xayariboun, and L. J. Butler, *J. Chem. Phys.* **92,** 823 (1990).
14. W. C. Wiley and I. H. McLaren. *Rev. Sci. Instrum.* **26,** 1150 (1955).
15. J. L. Franklin, P. M. Hierl, and D. A. Whan, *J. Chem. Phys.* **47,** 3148 (1967).
16. Y. Jiang, M. R. Giorgi-Arnazzi, and R. B. Bernstein, *Chem. Phys.* **106,** 171 (1986).
17. A. Gedanken and M. D. Rowe, *Chem. Phys. Lett.* **34,** 39 (1975); A. Gedanken, *Chem. Phys. Lett.* **137,** 462 (1987).
18. S. J. Riley and K. R. Wilson, *Faraday Discuss. Chem. Soc.* **53,** 132 (1972). W. P. Hess, S. J. Kohler, H. K. Haugen, and S. R. Leone, *J. Chem. Phys.* **84,** 2143 (1986).
19. T. F. Hunter and K. S. Kristjansson, *Chem. Phys. Lett.* **58,** 291 (1978).

Syage